

## LONG-TERM MEMORY OF THE HYDROLOGICAL CYCLE AND RIVER RUNOFFS IN CHINA IN A HIGH-RESOLUTION CLIMATE MODEL

RICHARD BLENDER\* and KLAUS FRAEDRICH

*Meteorologisches Institut, Universität Hamburg, Bundesstrasse 55, D-20146 Hamburg, Germany*

*Received 31 January 2005*

*Revised 16 January 2006*

*Accepted 1 February 2006*

### ABSTRACT

The hydrological cycle in China is analysed on the basis of a 250-years present-day climate simulation with a high-resolution (T63,  $\approx 2^\circ \times 2^\circ$ ) coupled atmosphere-ocean circulation model (ECHAM5/MPI-OM). The analysis of the annual data in the model simulation reveals long-term memory (LTM) on decadal time scales in some components of the hydrological cycle. LTM is characterised by a scaling exponent  $\beta > 0$  in the power spectrum  $S(f) \sim f^{-\beta}$  for low frequencies  $f$  and is determined by detrended fluctuation analysis (DFA). The simulated annual precipitation and atmospheric near-surface temperature fields show, as in the observations, a white low-frequency spectrum and, hence, no long-term memory in East Asia. However, simulated river flows of the Yangtze and the Huang He reveal LTM with scaling exponents  $\beta = 0.3\text{--}0.4$  (similar to the observations and that of the river Nile) extending beyond the decadal time scale. The model soil temperature indicates restricted memory up to time scales of approximately 30 years. In addition, the model's soil wetness, evaporation, and local runoff show memory on this time scale in a zonal belt at the latitude of Mongolia. Copyright © 2006 Royal Meteorological Society.

KEY WORDS: hydrological cycle; runoff; China; Tibet; climate variability; long-term memory

### 1. INTRODUCTION

The hydrological cycle is of predominant importance for vegetation and human living conditions and, therefore, climate is traditionally characterised by the availability of water. Not only averages but also, and even more so, the variability of hydrological processes determine the constraints for flora and fauna. This is especially relevant in areas with large populations like the eastern part of China, where the climate depends on the interactions of high, snow covered orography, an adjacent warm sea surface, and the resulting circulation. Teleconnections with the remote circulation in central Asia, the tropical Pacific and even the North Atlantic are suggested (Lin and Yin, 2001). Since observational data is scarce and of restricted duration, simulations with complex climate models provide, after verification, a unique tool for obtaining full spatial coverage, long-term behaviour, and estimates of possible anthropogenic climate change.

During the recent decades the hydrological cycle and associated processes have shown large trends and interannual variability. A prominent signal is the occurrence of floods, which show a substantial increase in frequency during the twentieth century (Milly *et al.*, 2002). Near-surface temperature and humidity at stations in China during 1961–1990 show an increase, which can be attributed either to an anthropogenic origin or to natural low-frequency variability (Wang and Gaffen, 2001). The decadal variability of droughts in 50 years NCEP reanalyses shows marked differences from a red noise process (Bordi *et al.*, 2004a,b; Bordi and Sutera, 2004).

---

\* Correspondence to: Richard Blender, Meteorologisches Institut, Universität Hamburg, Bundesstrasse 55, D-20146 Hamburg, Germany; e-mail: blender@dkrz.de

Low-frequency variability has been documented for the dryness/wetness index derived from historical records in the last 530 years by Qian *et al.* (2003a) and in the last 1000 years by Jiang *et al.* (1997) in Eastern China. The index of Qian *et al.* (2003b) reveals distinct centennial variability of the spatial patterns obtained by rotated empirical orthogonal function decomposition. The main characteristics of the long-term variability time series are supported by the precipitation in Beijing (1840–2000) and the Yangtze river runoff (1865–2000). The seasonal temperature in China, reconstructed for the last 500 years using historical documents and regression with observations, shows spectral peaks at 200, 80, 30, and 22 years (Wang *et al.*, 1991). A surprising result for the relation between precipitation predictability in China and the surface conditions like temperature, snow cover and soil moisture has been found in a series of model simulations (Liang *et al.*, 2002). In contrast to widespread presumptions, the impact of the dynamic initial conditions appears to be of major importance, suggesting the inclusion of the dynamical regimes. Global warming simulations predict an increase in the frequency of floods (Milly *et al.*, 2002). The East Asian summer monsoon intensifies and, owing to storage in the catchment during winter, the Yangtze discharge increases during summer (Bueh *et al.*, 2003).

The climate and the hydrological cycle in Southeast Asia indicate several remote lag relationships, which hint at climate mechanisms and potential predictability. For the Eurasian winter climate, the state of the Siberian-high plays the role of a centre of action and is negatively correlated with the mean temperature and precipitation in middle Asia (Gong and Ho, 2002). The last 20 years have shown a weakening of the corresponding regional mean sea level pressure, possibly related to snow conditions. A useful teleconnection exists between the Tibetan winter snow–cover anomalies and the summer precipitation, as recently demonstrated by Qian *et al.* (2003b) in the snow and rainfall observations during 1957–1998 and regional climate model simulations. An increase of snow cover and depth leads to a delay of the summer monsoon and a decrease of precipitation in southern China. That is, the interactions among snow, soil moisture, and surface temperature, accompanied by altered heat and moisture fluxes, and ultimately, by a changing atmospheric circulation describe the underlying process. Furthermore, the Mongolian snow depth is related to the North Atlantic Oscillation (NAO) and the Eurasian teleconnection pattern (EA) (Moringa *et al.*, 2003). Observations at 23 stations (1940–1992) reveal spatial structures that are correlated with preceding NAO and EA time series, indicating a potential for long-range predictability.

Information about the mean and the variability of the hydrological cycle suffers from lack and uncertainty of observations. The uncertainty of precipitation measurements in monthly means of six data sets leads to the conclusion that accurate observations are required for runoff estimates, in particular, in arid and semi-arid regions (Fekete *et al.*, 2004). Large differences between different observational data sets are reported for the hydrological cycle in the tropics (Roads, 2003). Therefore, the unreliability of data may not be sufficient cause to dismiss simulated results.

A long-term memory (LTM) of the near-surface temperature has been found by Fraedrich and Blender (2003) and Blender and Fraedrich (2003) in global observations and coupled atmosphere ocean simulations for the present-day control runs and scenario forcings. Scaling of the power spectrum (measured by the fluctuation function) is shown up to centennial time scales, i.e.  $S(f) \sim f^{-\beta}$  with exponents  $\beta \approx 1$  over the oceans and  $\beta \approx 0$  on the inner continents. This type of analysis was restricted to the near-surface temperature. LTM hampers the statistical description of time series.

The aim of this paper is to analyse the LTM (equivalent to enhanced low-frequency variability) of the hydrological cycle and the processes involved in China and the neighbouring areas. Since such a study is not possible on the basis of observations, a long-term simulation ( $\approx 300$  years) with a high-resolution ( $\approx 2^\circ \times 2^\circ$ ) coupled atmosphere–ocean climate model is used as a data basis. The atmospheric model is ECHAM5 with improvements of the land surface processes (Roeckner *et al.*, 2003), which is coupled to the ocean model MPI-OM without flux correction. This present-day simulation is part of a series of sensitivity studies for the IPCC (Jungclaus, 2006) and will be compared with different scenario simulations. We derive features of the low-frequency variability of the atmospheric near-surface temperature, soil temperature, soil wetness, snow depth, precipitation, evaporation, and runoff with the detrended fluctuation analysis (DFA) in East Asia/China and consider the behaviour at individual locations in Tibet and Mongolia in detail. To concentrate on the interannual variability the analysis is restricted to annual means. The low-frequency variability of the model

can be verified with observed patterns for the near-surface temperature and precipitation. Furthermore, the river flows of the Yangtze and the Huang He as produced by the model can be compared to available observational data. The study predicts LTM properties that are relevant for model evaluation, the understanding of the natural variability, parameterisation, the construction of simple models, and the assessment of anthropogenic scenario simulations.

In Section 2, the model and the observed data are described. The main properties of LTM and the application of the detrended fluctuation analysis (DFA) are outlined in Section 3. The LTM of the simulated hydrological cycle and the observed river runoffs is presented together with hints on possible underlying mechanisms in Section 4. In Section 5, the results are summarised and discussed. In the Appendix, the hydrological cycle of the model is compared with the NCEP reanalysis data.

## 2. MODEL AND DATA

The atmospheric model ECHAM5 (Roeckner *et al.*, 2003) is used to simulate a present-day climate control run for 308 years (the initial 50 years are neglected). The resolution is triangular T63 ( $\approx 2^\circ \times 2^\circ$ ) with 31 vertical levels. The atmospheric model is coupled with the ocean model MPI-OM (based on C-HOPE, see Wolff *et al.* (1997) and Legutke and Maier-Reimer (1999)) with  $1.5^\circ$  resolution without flux correction.

Compared to the previous version ECHAM4, several major changes that improve the hydrological cycle are included. The most relevant are a semi-Lagrangian transport scheme for water components, new cloud parameterisations, and new representations of land surface processes (Hagemann and Dümenil-Gates, 2003). The land surface model is based on high-resolution ( $0.5^\circ$ ) data with parameterisations derived from the statistical properties of topography data with a 1-km resolution. In the present study, the hydrological cycle is described by the surface climate, water reservoirs, and fluxes: 2 m temperature, soil temperature (in the upper layer, 0.065 m), soil wetness, snow depth, precipitation, evaporation, and runoff. Inspection of the time series indicates that the model undergoes an initial spin up trend during the initial 50 years, which is neglected, leading to 250 years for the analysis.

Compared to the previous model versions, the most relevant changes of the parameterisations for the present study are as follows:

1. Soil temperature diffuses within the upper 10 m in five layers with uneven spacing (the uppermost layer has 0.065 m) and zero flux at the bottom. Heat capacity and diffusivities are heterogeneous and defined according to a soil map.
2. Soil water is stored in a bucket with heterogeneous capacity and gets changed by rainfall, evaporation, snow melt, surface runoff, and drainage. The individual grid cells are characterised by a probability distribution of the storage capacity. To represent the variability of the orography below the grid resolution, additional parameters are included at each cell.
3. The local runoff field is determined by a complex algorithm using the subgrid scale properties of the surface. The main characteristic is a distribution for the storage capacity, which leads to a modification of the traditional bucket approach; this is attained only for completely saturated grid cells.

The analysed region is East Asia/China in 60E–150E and 10N–60N, with Yekaterinburg and Kamtschatka at the western and eastern boundaries in the north, and the Arabian Sea and the Mariana Islands in the south. This region includes climatologically different areas like the Siberian lowlands and the Gobi desert, the high altitudes in Mongolia and the Himalayas, as well as the highlands of Manchuria and southeast China. Snow covered areas are found in Mongolia and Tibet and the largest part of the runoff is channelled to the Yangtze and the Huang He rivers.

The model verification based on NCEP reanalysis data (Kalnay *et al.*, 1996) is described in the Appendix.

Annual river flow data for the Yangtze (Chang Jiang) and the Huang He (Yellow river) are obtained from the Global Runoff Data Centre (GRDC). The river flow of the Yangtze is measured at the stations Hankou for 1865–1986, and at Yichang for 1882–1986. The flow measurements of the Huang He are a combination

of the data at station Shanxian for 1919–1958 and the station Sanmenxia for 1953–1988. The overlap from 1953–1958 shows sufficient correspondence to allow joining the time series for 1919–1988.

### 3. LONG-TERM MEMORY AND DETRENDED FLUCTUATION ANALYSIS

LTM is present if the low-frequency variability grows with decreasing frequency. LTM is defined by the non-integrability of the correlation function  $C(t)$ , which requires that for a power law,  $C(t) \sim t^{\beta-1}$ , the exponent  $\beta$  is within the range  $0 < \beta < 1$  for long time lags  $t$ . This correlation function corresponds to a power spectrum that is white for  $\beta = 0$ , whereas for  $\beta = 1$ , the time series becomes non-stationary with  $1/f$  spectrum (or flicker noise).

LTM can be analysed by DFA, which has been developed to analyse non-stationary time series (Peng *et al.*, 1994). The DFA has been extended for the analysis of time series with superimposed trends of any polynomial shape (see e.g. Govindan *et al.* (2002), Fraedrich and Blender (2003)). This is relevant if variability needs to be excluded for time scales of the order of the total length. An important application is the analysis for anthropogenic signals or natural variability (Blender and Fraedrich, 2003).

The major application of the DFA is the extraction of power laws while oscillations (or cycles) appear as steps in the fluctuation function with a time scale corresponding to the period (Fraedrich, 2002). The superposition of several different periodicities may lead to erroneous power laws. In order to avoid such misinterpretations, the DFA results are compared with a power spectrum. In the present study, the power spectra are averages of the spectra calculated in seven overlapping segments.

The result of the DFA is the fluctuation function  $F(t)$  measuring fluctuations of the time series on time scales  $t$ . In the case of a power law in the power spectrum,  $S(f) \sim f^{-\beta}$ , there is the relation  $F(t) \sim t^\alpha$ , with  $\beta = 2\alpha - 1$ . Analogously, the correlation function  $C(t)$ , which is directly related to the spectrum, follows the power law decay  $C(t) \sim t^{\beta-1}$ . The method is implemented as follows. First, the anomalies are integrated to the so-called profile. The fluctuation function  $F(t)$  is calculated by partitioning the profile time series in segments of duration  $t$ ; linear fits are determined separately for each segment. The fluctuations  $F(t)$  are the means of the variances of the profile with respect to the fits. If trends or higher-order polynomial growth types are present in the original time series, then, instead of linear fits, polynomials of order  $N$  are fitted and subtracted in the segments and the method is defined as DFA- $N$  (the original version is DFA-1). Note that DFA-1 does not eliminate linear trends in the original time series. In the present study the main results are based on DFA-1, which are compared with DFA-2 and DFA-3 to detect possible long-term trends.

There is no statistical theory underlying the power law exponents of the DFA, and hence it is not possible to determine the significance. Therefore, in order to gain an estimate for the fluctuation of exponents in typical climatological data, Fraedrich and Blender (2003) determined a sample of exponents in 100-year segments of a 1000-year coupled simulation. Global maps of the variance suggest an uncertainty  $\approx 0.05$  of  $\alpha$ , which is considered as a lower bound. Hence we assume an uncertainty of at least 0.1 for the spectral exponent  $\beta$ . The exponents  $\alpha$  and  $\beta$  are determined within the decadal time range and calculated as the slope within 5–40 years. Independent analyses of the grid point time series yield the geographical distributions of fluctuation exponent determined by DFA-1.

### 4. CLIMATOLOGY OF LONG-TERM MEMORY

LTM is first analysed for state variables, which characterise the water cycle, near-surface and soil temperature, soil wetness, and snow depth. Thereafter, the fluxes, described by the water balance, precipitation, evaporation, and runoff, are subjected to LTM analysis. Owing to the duration of 250 years, significant results can be obtained up to several decades. While this cannot be verified within reanalysis data, this is possible for instrumental river runoff observations, which are available for more than 100 years.

#### 4.1. Long-term memory of temperature, wetness, and snow depth

4.1.1. *Near-surface (c) temperature.* The low-frequency variability spectrum of the near-surface temperature, T2m, shows a weak LTM (Figure 1(a)). In wide areas, the spectrum is white ( $\alpha \approx 0.5$ ) indicating no

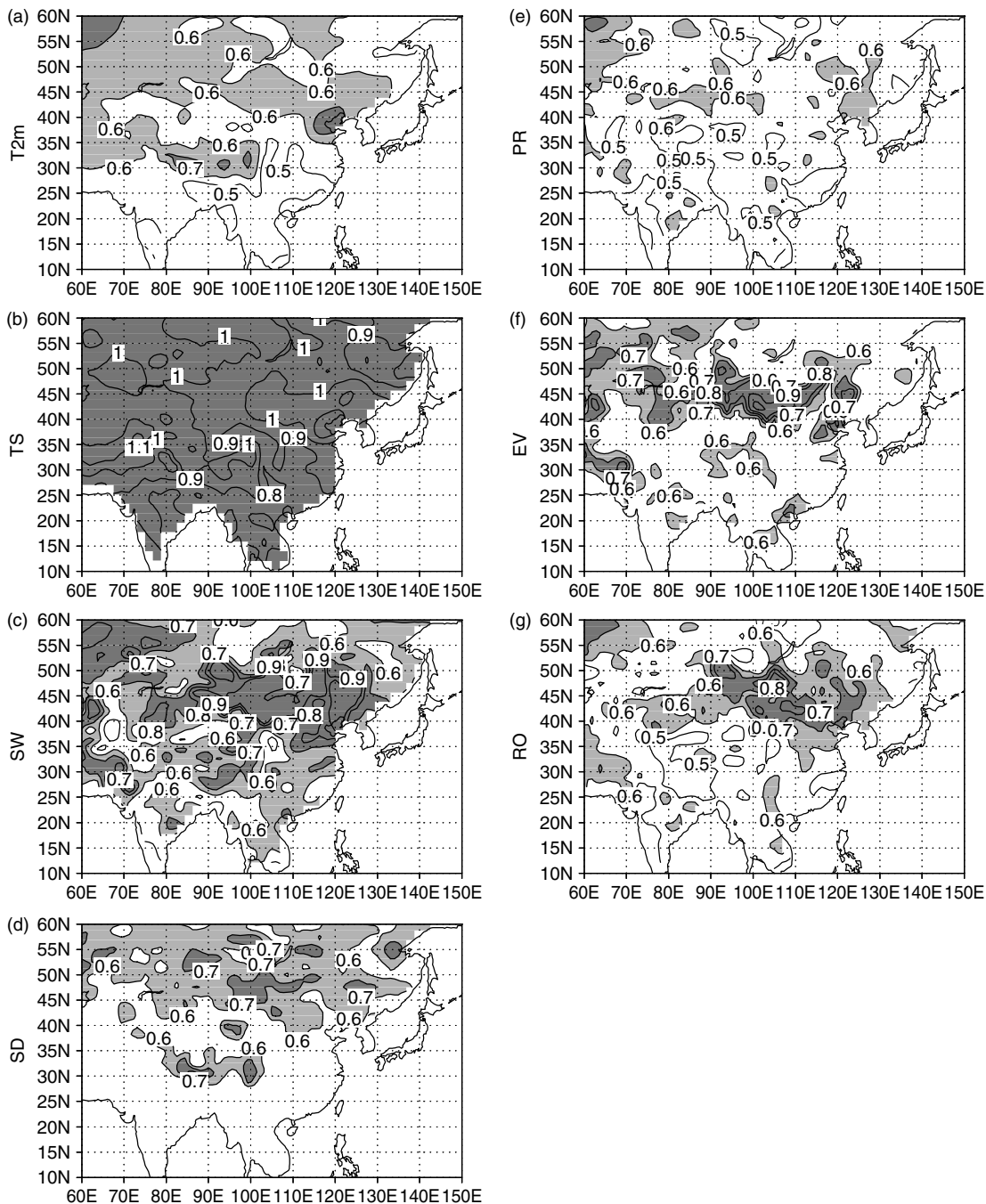


Figure 1. Power law exponent  $\alpha$  of the fluctuation function obtained by DFA-1 for (a) the near-surface temperature T2m, (b) soil temperature, (c) soil wetness, (d) snow depth, (e) precipitation, (f) evaporation, and (g) runoff.  $\alpha$  is obtained by a fit in 5–40 years, and values  $0.6 < \alpha < 0.7$  are shaded light, above  $\alpha > 0.7$  shaded dark

memory beyond 5 years. Global analysis (not shown) reproduces the distribution in observations and simulations (Fraedrich and Blender, 2003) with  $\alpha = 1$  (or  $1/f$ -spectrum) over the oceans and no memory over the inner continent. The weak LTM found in the northwest of Figure 1(a) is a branch of the memory in the Arctic sea (not shown).

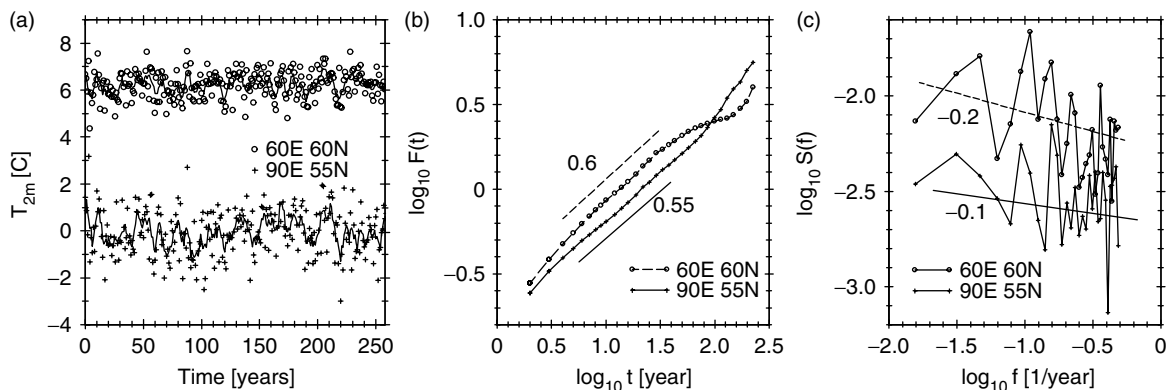


Figure 2. Near-surface temperature in 60E, 60N (○) and 90E, 55N (+): (a) annual means and decadal averages (solid), (b) fluctuation functions  $F(t)$  (compare Figure 1(a)), and (c) power spectra. In (b) the lines indicate the slopes  $\alpha = 0.55$  and  $0.6$  in 5–40 years, in (c) the corresponding spectral slopes in  $S(f) \sim f^{-\beta}$  are  $-0.1$  and  $-0.2$  (using  $\beta = 2\alpha - 1$ )

In Figure 2, the analysis of time series at the grid points near 60E, 60N and 90E, 55N (Figure 2(a)) is presented. In 60E, 60N the fluctuation spectrum (Figure 2(b)) shows a power law with the exponent  $\alpha = 0.6$  (with slightly increasing values for higher order DFA). The shape of the fluctuation function indicates a change to white noise ( $F(t) \sim t^{0.5}$ ) at the period of roughly 30 years. The DFA spectra in 90E, 55N show the power law  $\alpha = 0.55$ , in all DFA versions, with insignificant deviations above 100 years. The agreement between all curves is a reliable hint at power law scaling related to self similar memory. Since in both areas the power spectra (Figure 2(c)) do not show periodicities, this result indicates power law scaling of the near-surface temperature with weak LTM.

**4.1.2. Soil temperature.** The temperature of the upper soil layer follows a soil diffusion equation with heat fluxes depending on radiation and moisture exchange. The pattern of the fluctuation function exponent (Figure 1(b)) shows a nearly homogeneous distribution with  $\alpha \approx 1$ . As an example of the behaviour within this homogeneous pattern, a grid point in Tibet (near 90E, 30N) is chosen (Figure 3). The fluctuation functions (Figure 3(b)) reveal a gradual increase with roughly  $F(t) \sim t$  up to decades, and a lower value for the exponent beyond decades. The power spectrum (Figure 3(c)) reveals that a power law fit is not possible since the slope  $-0.8$  appears as a transition between white and steeper spectra. The whole spectrum is most probably of Lorentzian type,  $1/[f_0^2 + f^2]$ , with a characteristic frequency  $f_0$  and a wide transition region.

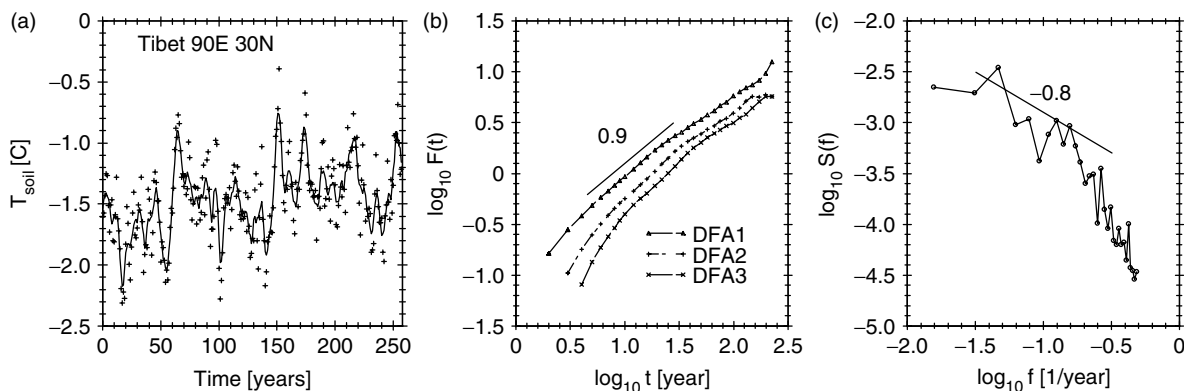


Figure 3. Soil temperature in Tibet (90E, 30N): (a) annual means and decadal averages (solid), (b) fluctuation functions  $F(t)$  for DFA versions 1, 2 and 3 (for DFA-1 compare Figure 1(b)), and (c) power spectra. In (b) the line indicates the slope  $\alpha = 0.9$  in 5–40 years, the corresponding slope in (c) is  $-0.8$

This is consistent with the high frequency spectrum of an AR(1) process. Although a characteristic time scale may not be well defined, a rough estimation yields several decades as found for the near-surface temperature.

**4.1.3. Soil wetness.** The power law exponent for the soil wetness is displayed in Figure 1(c). The spectrum hints at large exponents,  $\alpha \approx 1$ , in Northeast China. South of 35N and north of 55N the memory decays to values comparable with white noise. To elucidate this apparent LTM, the detrended fluctuation analysis and the power spectrum are applied to a particular time series in Mongolia (Figure 4, 100E, 45N). The fluctuation function  $F(t)$  (Figure 4(b)) increases with an exponent  $\alpha \approx 1.5$  for time scales below 30 years and bends to white noise above (the latter is not significant), which appears synchronously in all the DFA versions. The power spectrum (Figure 4(c)) shows clearly that the time series is well described by a Lorentzian spectrum with a time scale of approximately 30 years. We attribute this memory to the water storage, which can be considered to be independent of fast precipitation, evaporation, and runoff. Note that the time series appear to be non-stationary up to 30 years. The LTM in Tibet (Figure 5, 90E, 30N) is weak with  $\alpha \sim 0.65$  and  $\beta \sim 0.3$  (Figures 5(b,c)).

**4.1.4. Snow depth.** Snow cover in Tibet and Mongolia plays a major role for the climate of China. Snow depth shows weak LTM in Tibet and northern China (Figure 1(d)) with exponents  $\alpha$  up to 0.7.

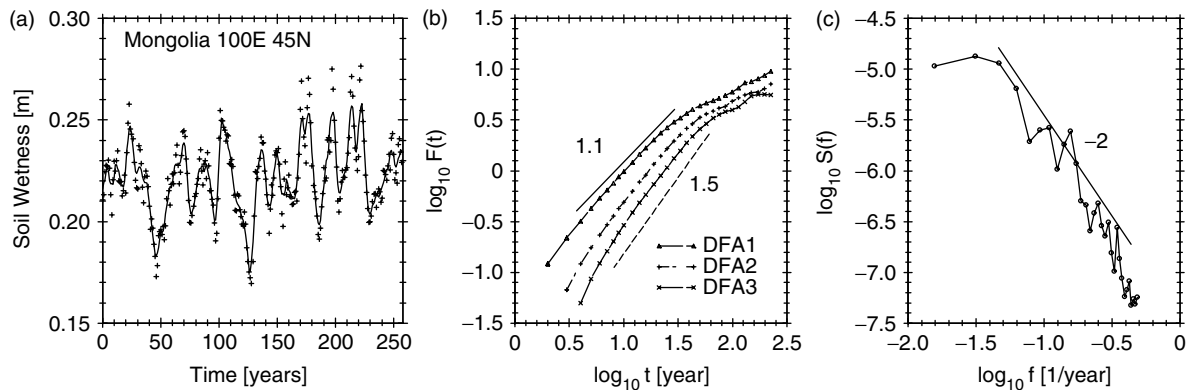


Figure 4. Soil wetness in Mongolia (100E, 45N): (a) annual means and decadal averages (solid), (b) fluctuation functions  $F(t)$  for DFA versions 1, 2 and 3 (for DFA-1 compare Figure 1(c)), and (c) power spectrum. In (b) the lines indicate slopes  $\alpha = 1.1$  and 1.5 in 5–40 years, in (c) the corresponding slope is  $-2$  for  $\alpha = 1.5$

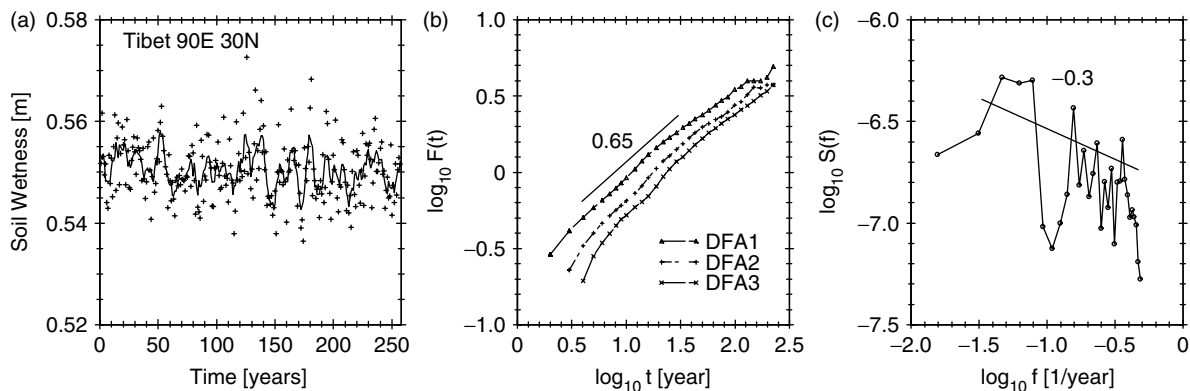


Figure 5. Soil wetness in Tibet (90E, 30N): (a) annual means and decadal averages (solid), (b) fluctuation functions  $F(t)$  for DFA versions 1, 2 and 3 (for DFA-1 compare Figure 1(c)), and (c) power spectrum. In (b) the line indicates slope  $\alpha = 0.65$  in 5–40 years, in (c) the corresponding slope is  $-0.3$

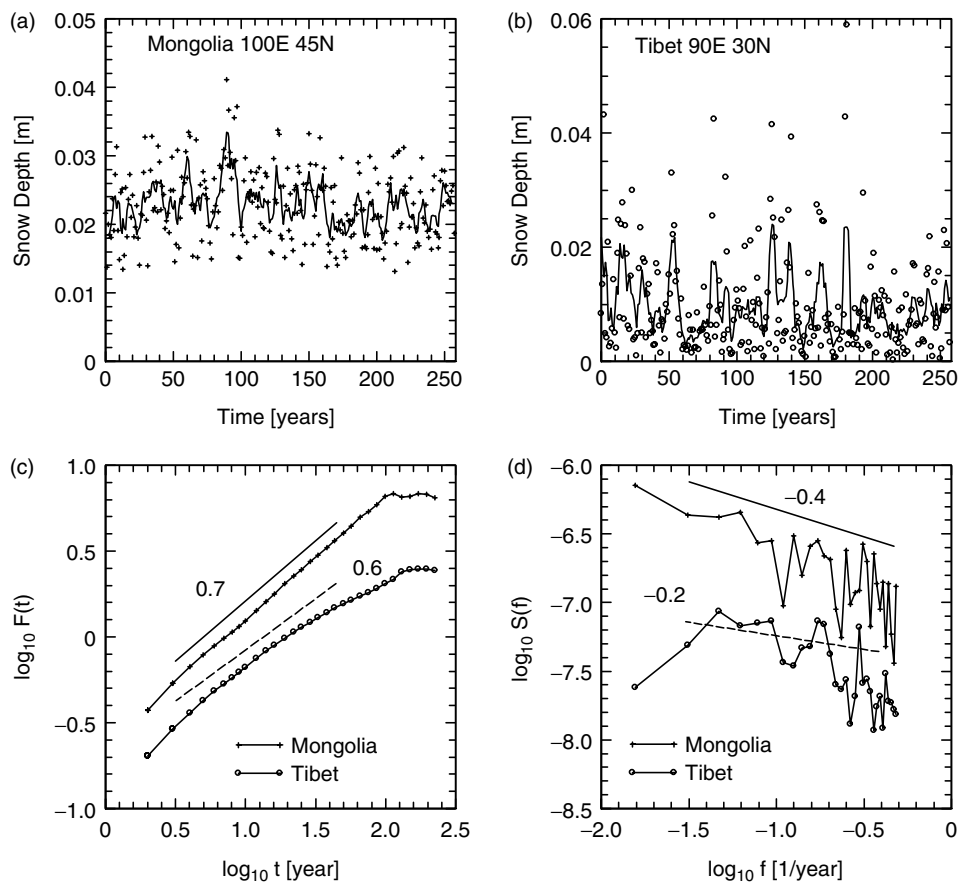


Figure 6. Snow depth in (a) Mongolia (100E, 45N, +) and (b) Tibet (90E, 30N, O). (c) Fluctuation functions  $F(t)$  obtained by DFA-1 (compare Figure 1(d)) and (d) power spectra. The lines in (c) indicate the exponents  $\alpha = 0.7$  (solid) and  $\alpha = 0.6$  (dashed) in 5–40 years; the corresponding slopes in (d) are  $-0.4$  and  $-0.2$ .

Two representative areas in Mongolia (100E, 45N) and Tibet (90E, 30N) with high values are analysed in detail (Figure 6). In Mongolia, the fluctuation function (Figure 6(c)) scales with an approximate exponent  $\alpha = 0.7$  supported by the power spectra with a scaling exponent  $\beta = 2\alpha - 1 = 0.4$  (Figure 6(d)). However, the behaviour in Tibet in the frequency range below 1/30 years remains unclear in the DFA-1 analysis (Figure 6(c)); the power spectrum is reconcilable with a Lorentzian or even with a white spectrum (Figure 6(d)). Hence we conclude that this variable carries no LTM according to the simulation. The latter finding is highly relevant since the Tibetan snow depth is considered to be a central agent in the East Asian climate.

In summary, the storage compartments' soil temperature and wetness show scaling behaviour and LTM in the transition time range of 5–40 years, which is most clearly developed in the region of northern China/Mongolia. Snow depth reveals weaker memory, particularly in the Tibet/Himalaya region.

#### 4.2. Long-term memory of precipitation, evaporation, and runoff

**4.2.1. Precipitation.** The memory properties of precipitation are of predominant interest and are accompanied by the hope for potential predictability. However, the analysis within 5–49 years reveals fluctuation exponents,  $\alpha \approx 0.5$ , in the simulated precipitation field (Figure 1(d)), with small areas with slightly higher values. The small extent of these areas and their lack of spatial correlations agree with the hypothesis that

precipitation shows no LTM on the time scales beyond a year. That is, precipitation is characterised by a white noise mechanism in the hydrological cycle, which is found everywhere on the globe (not shown).

**4.2.2. Evaporation.** The evaporation depends on soil moisture and soil temperature. Large values of the fluctuation exponent are found in a zonal belt in 40–50N with maxima in Mongolia. These areas coincide with the areas of LTM of the soil wetness (Figure 1(e)). Inspection of the evaporation time series in Mongolia 100E, 45N (Figure 7) shows a steep increase of the fluctuation function (Figure 7(b)) up to several decades ( $\alpha \approx 0.85$ ). The different slope obtained by DFA-3 ( $\alpha = 1$ ) indicates non-stationarity. According to the power spectrum (Figure 7(c)) a Lorentzian spectrum with the threshold of roughly 30 years cannot be rejected; this coincides with the spectral behaviour of the soil wetness (Figure 4(c)).

**4.2.3. Runoff.** For runoff, the distribution of the fluctuation exponent  $\alpha$  (Figure 1(f)) shows LTM patterns similar to soil wetness and evaporation. The magnitude of the exponent and the region with discernible values, however, are smaller. Largest values of the exponent occur in Mongolia, 100E, 45N (Figure 8) where the time series (Figure 8(a)) leads to a fluctuation function (Figure 8(b)) as well as a power spectrum (Figure 8(c)), which indicate LTM on time scales beyond 30 years.

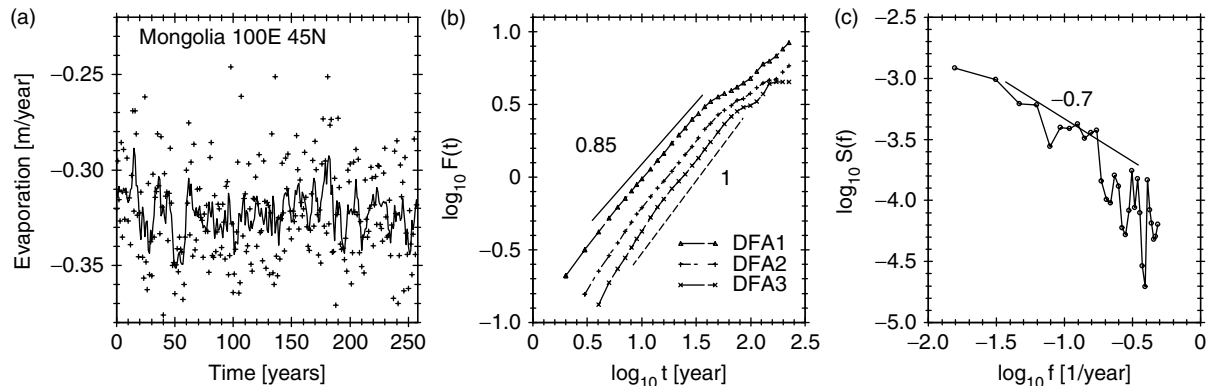


Figure 7. Evaporation in Mongolia (100E, 45N): (a) time series and decadal average (solid), (b) fluctuation functions  $F(t)$  obtained by DFA versions 1, 2 and 3 (see also Figure 1(f) for DFA-1) with slopes  $\alpha = 0.85$  and 1 in 5–40 years, (c) power spectrum with slope  $-0.7$  for  $\alpha = 0.85$

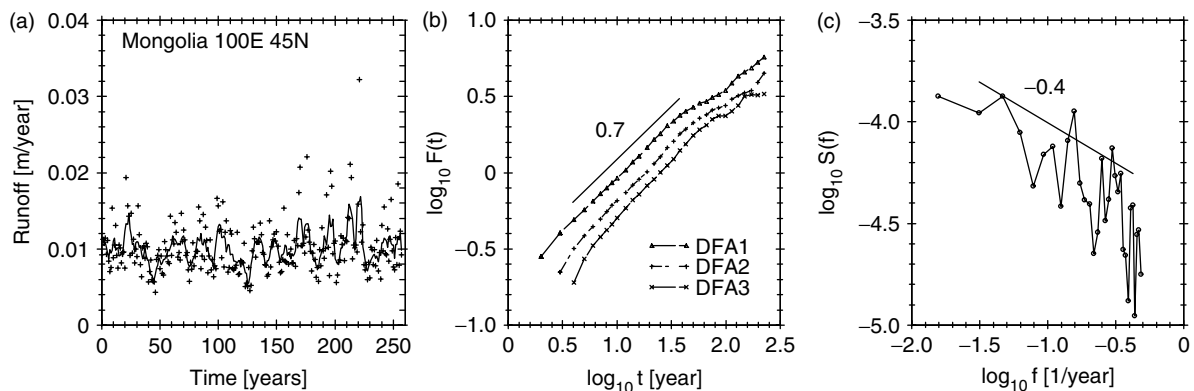


Figure 8. Runoff in Mongolia (100E, 45N): (a) time series and decadal average (solid), (b) fluctuation functions  $F(t)$  obtained by DFA versions 1, 2 and 3 (see also Figure 1(g) for DFA-1) with slope  $\alpha = 0.7$  in 5–40 years, (c) power spectrum with the corresponding slope  $-0.4$

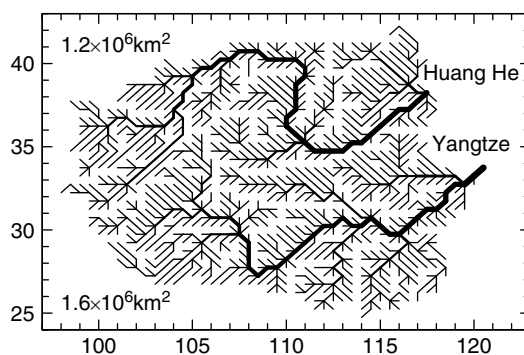


Figure 9. Flow geometry in the catchments of the Yangtze and the Huang He. The line thickness is proportional to the square root of the flow; catchment areas are included

#### 4.3. Long-term memory of river discharges

The model river flow is the estuary discharge, determined by the agglomerated runoffs in the catchment. The two catchments are shown in Figure 9. The flow elements are determined by a simple downward gradient approach in the half degree resolution orography used by the model. To indicate the possible flow intensities, the thickness of every line is determined by the square root of the total agglomerated flow for homogeneously distributed precipitation. This graphical procedure is applied independently for each river and the thickness is scaled by the maximum obtained as the estuary outflow. The model river flow is given by the runoff at the last grid point on the coast (discharge). Whereas the Yangtze catchment encompasses the realistic size ( $\approx 1.7 \times 10^6 \text{ km}^2$ ), the observed Huang He catchment ( $\approx 0.7 \times 10^6 \text{ km}^2$ ) is overestimated by this analysis. The fluctuations of river fluxes have been analysed by Livina *et al.* (2003). On time scales below 1 year the power spectra of 30 rivers show power law scaling,  $S(f) \sim f^{-\beta}$  with  $\beta = 0.3 \dots 0.7$ . This analysis by Livina *et al.* concentrates on European rivers, and Chinese catchments are not included. The LTM of the outflows of the Yangtze and the Huang He are analysed and compared with observations, which are available for the Yangtze after 1865 and for the Huang He after 1919. This is the most relevant verification of the present study.

Figure 10 shows the observed discharges of the Yangtze in Hankou and Yichang (Figure 10(a)) and the Huang He (Figure 10(b)). The observed magnitudes are overestimated by the simulation (Figure 10(c)), which is due to the monsoon circulation being too strong in ECHAM5. The fluctuation functions of the available flows of the two rivers are compared with the corresponding outflow in the present ECHAM simulation. For the Yangtze (Figure 10(d)), the observations yield  $\alpha = 0.7$  (Hankou), and 0.65 (Yichang), in agreement with  $\alpha = 0.65$  of the simulation. For Huang He (Figure 10(e)), the analysis of the combined data yields  $\alpha = 0.65$  as in the simulation. Obviously, despite the overestimated discharge, the simulated non-trivial scaling of the simulation agrees with observations up to time scales of decades. Owing to the sampling, longer time scales cannot be analysed by observations, but the simulation indicates that the scaling behaviour continues to longer time scales.

This result is not supported by the memory properties as obtained by the soil, which indicates a finite memory of decadal time scale. A clear decision cannot be made, given the finite simulation time, but it is likely that the river flows show longer time scale memory and related scaling compared to the soil processes involved. It is possible that the snow depth and evaporation in Mongolia supply the LTM.

#### 4.4. On mechanisms

The variety of the spectra and the scaling exponents obtained for the hydrological variables in the different regions hint at the absence of a single underlying linear process.

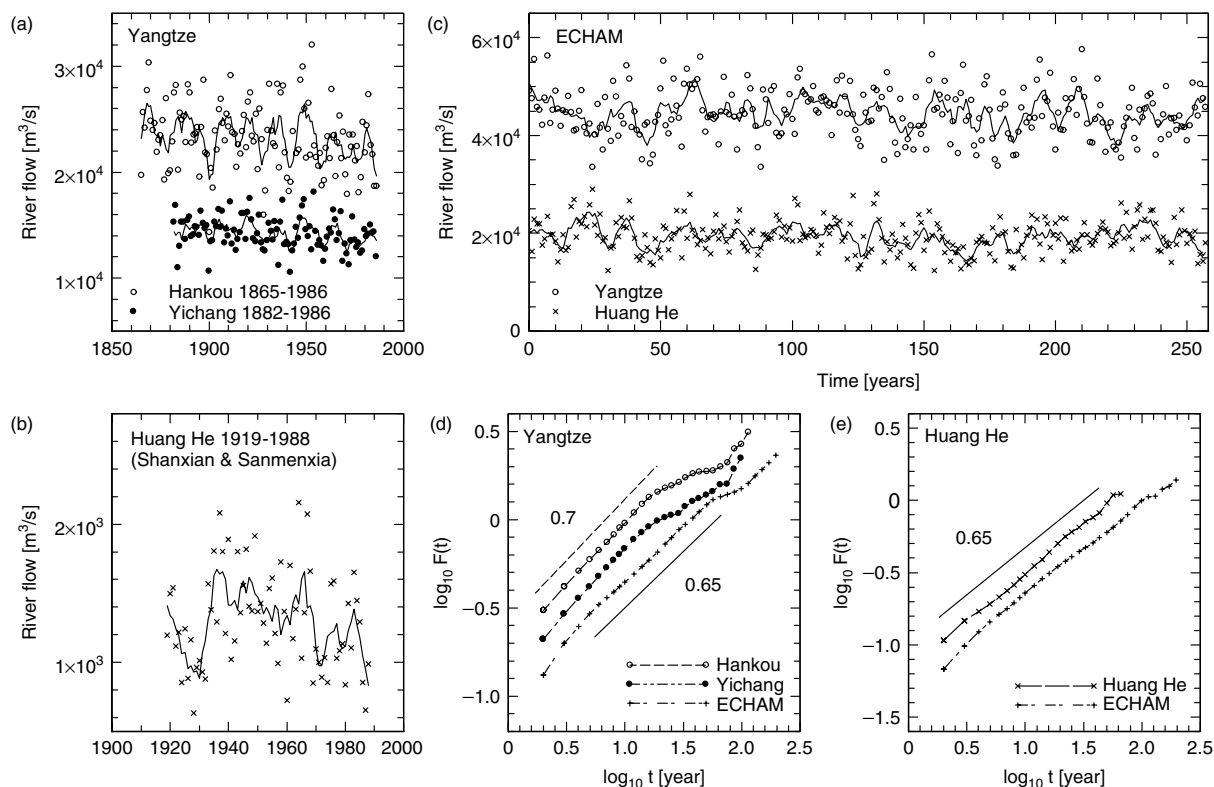


Figure 10. Observed flows of (a) the Yangtze in Hankou (○, 1865–1986) and Yichang (●, 1882–1986), and (b) the Huang He (×, combination of stations Shanxian and Sanmenxia, 1919–1988). (c) ECHAM simulation of the Yangtze (○) and the Huang He (×). Observed fluctuation functions for the Yangtze (d) in Hankou (○) and Yichang (●) and the Huang He (e) compared with the simulated flows (+). The lines indicate exponents 0.65 (solid) and 0.7 (dashed)

In general, fractional exponents may originate from models with distinct non-linearity in the feedbacks. However, this explanation is of restricted value for interpretation and understanding, since it does not lead to basic and comprehensible concepts.

Two common linear models that produce non-trivial, fractional scaling exponents are as follows:

- (1) Linear diffusion models with two compartments (as in Fraedrich *et al.* 2004) may explain the half integer exponents  $\beta = 1/2, 1, 3/2, 2, \dots$  for particular parameter ranges. However, there is no comparable mechanism implemented in the soil model, which could simulate this two layer diffusion (the five level soil temperature diffusion is not sufficient to parameterise a continuous diffusion). Nevertheless, this may be possible in nature.
- (2) Superposition of several Lorentzian spectra with different characteristic frequencies serves as a model for the interaction of linear processes with different time scales. Given the data available in the present study, such a superposition cannot be rejected. The investigation of such a mechanism would require a thorough analysis of the simulated processes with emphasis on the linearisations of the otherwise non-linear parameterisations of the water cycle and soil processes.

To explain the power spectra by a concise analytical expression, a simple modification of the Lorentzian spectrum is proposed. To account for the non-trivial scaling of the spectra, a power of the frequency is included in the ordinary Lorentzian spectrum

$$S(f) \approx \frac{S_0}{1 + (f/f_0)^\beta} \quad (1)$$

Table I. Spectral exponents  $\beta$  in Equation (1) within 5–40 years for the hydrological variables in the two regions Tibet, Mongolia, and a rough estimate for the remaining area (where available)

Spectral exponent $\beta$	Tibet	Mongolia	Rest
2m temperature	0.3	0.3	0
Soil temperature	1	1	1
Soil wetness	0.3	0.5	0.3
Snow depth	0.2	0.4	(0.3)
Precipitation	0	0	0
Evaporation	0	0.7	0
Runoff	0	0.4	0

with  $\beta = 2$  representing a Lorentzian shape. Noteworthy is the appearance of the climatological time scale  $1/f_0 \approx 30$  years, which emerges as a general feature for all components. The exponents  $\beta$  for the hydrological variables in the Tibetan region, Mongolia, and the remaining parts of China are summarised in Table I for the time scales within 5–40 years (Figure 1). Although for some variables these values characterise a transitional frequency band, they are relevant for a comparison with observations that, in general, are confined to this time range. The most noteworthy results are the complete absence of memory in precipitation, LTM of river runoff, and  $1/f$  – noise of soil temperature. However, owing to the finite simulation period, larger time scales cannot be excluded. Although it is not possible to prove the existence of the modified spectrum (1), this relation might be of practical value for parameterisations and for the development of simplified, conceptual models of long-term behaviour.

## 5. SUMMARY AND DISCUSSION

The hydrological cycle in China is analysed using a 250-year control simulation of the present-day climate. The simulation is performed with the atmospheric climate model ECHAM5 in a high resolution ( $\approx 2^\circ \times 2^\circ$ ) coupled to the ocean model MPI-OM (HOPE) without flux correction. Annual mean grid point time series are diagnosed with DFA and power spectra. A main result of the paper is that the precipitation time series are uncorrelated, corresponding to a white power spectrum without enhanced low-frequency variability. Therefore, the major driving mechanism of the hydrological cycle has no LTM and any memory observed in other variables must have its origin in water storage and flow properties. This is supported by simulations of Liang *et al.* (2002) relating the dynamic initial conditions to rainfall predictability in China, since these initial conditions can be considered as uncorrelated and spectrally white. The following results of our analysis should be noted.

First, the atmospheric near-surface temperature shows no substantial LTM in large areas, with modest values over the oceans, in Tibet, and in central Asia (the northeastern part of the analysed region). The soil temperature, on the other hand, reveals red noise with an approximate Lorentzian shape turning to white noise at a time scale of 30 years. This pertains to the whole region. The soil wetness varies geographically with weak memory, aside from Tibet and an extended region around Mongolia. While a weak red noise with  $\beta \approx 0.3$  is found in Tibet, a Lorentzian shape occurs in Mongolia.

The evaporation and the runoff show similar patterns of LTM, with considerable memory in Mongolia ( $\beta \approx 1$  for evaporation and  $\beta \approx 0.5$  for runoff), but vanishing memory in the remainder of China. LTM of snow depth is found in Mongolia and Tibet (maximum values of  $\beta \approx 0.4$ ). In Mongolia this extends possibly beyond the 30 years.

The rather weak LTM of snow depth indicates that the related storage capacity is of much less relevance than soil wetness, and that snow depth is not the major driving mechanism for LTM in river flows. The time scale of snow depth in high orography appears to be much lower than that of the soil wetness and indicates

that this water storage compartment is substantially driven by the fast atmospheric variables, temperature and precipitation.

Observed river flows provide a major verification for the simulated runoff. The two rivers, Yangtze and Huang He, show weak LTM  $\beta \approx 0.3$ , consistent in observations and the model simulations. The same result is found by Hurst (1951) in his famous analysis of the Nile river. Thus, the proper simulation of the observed river flow variability validates the complex model parameterisations involved.

The simulated river discharge indicates LTM with homogeneous scaling for time scales longer than 30 years. Most of the other processes relax to white noise beyond 30 years, which is another supporting factor for the traditional climatological averaging time.

The present analysis poses several questions. The first is the requirement for a simple model to explain the non-trivial scaling of LTM in soil wetness, evaporation, runoff, snow depth, and the river flows. A possible model with such scaling behaviour is investigated by Fraedrich *et al.* (2004) with application to the LTM of the sea surface temperature. Furthermore, the role of the biosphere is not considered here. In reality, vegetation introduces a short time scale, which is related to the seasonal climate variability and the lifetime of the individual plant, and a long time scale, which corresponds to the life time of the plant species and the vegetation composition. Although the observed scaling might be a transition that is valid in the 1–10-year band, some results indicate substantial deviations from Lorentzian spectra of the Brownian motion analogue. A further unexplored problem is the LTM found for evaporation and runoff in Mongolia and Tibet.

#### ACKNOWLEDGEMENTS

The authors thank U. Luksch for discussions and extracting the river flow data in the ECHAM simulation. They also appreciate fruitful discussions with S. Hagemann (Max-Planck-Institute for Meteorology, Hamburg) and the useful reports of the referees. The support by M. Botzet, E. Roeckner, and the Model and Data group is acknowledged. Financial support for this work was given by the Deutsche Forschungsgemeinschaft (SFB512 and FR450).

#### APPENDIX

##### *Comparison of ECHAM5 and NCEP climatologies*

To verify the model simulation, its hydrological cycle is compared with NCEP reanalyses (Kalnay *et al.*, 1996). The NCEP data considered here is a model output (besides  $T_{2m}$ ) and not assimilated using observations (therefore denoted as class C in the terminology). The hydrological cycle in the NCEP reanalyses has been compared with ECHAM and evaluated by Hagemann and Dümenil-Gates (2001).

This study revealed several deficiencies of the NCEP data, which are relevant for the present study. The first point is an error in the snowpack and the neglect of snowmelt in the runoff. Furthermore, the water balance is not closed at the land surface (owing to the nudging of soil moisture to climatology), which leads to negative P-E values in some regions. Deficiencies in the hydrological cycle are also present in the ERA40 reanalysis data Hagemann and Dümenil-Gates (2001). An advantage of the NCEP reanalysis is the realistic simulation of the discharge in the southern Asia monsoon region. Therefore, we use this data set since it represents a consistent simulation of the hydrological cycle (besides the deficiencies mentioned).

Climate means and standard deviations of the simulation are displayed in Figures 11 and 12 for the 2m temperature, soil temperature, soil wetness, snow depth, precipitation, evaporation, and runoff. Note that, since the variables considered in this study are not assimilated in NCEP (besides  $T_{2m}$ ), a stringent assessment of the simulation output is not possible.

In general, the model output agrees quantitatively with the NCEP data. This pertains to the means (Figure 13) as well as the year to year variabilities (Figure 14). However, the simulation reveals a higher degree of horizontal details compared to the smoother NCEP data. This appears to be most probably due to the detailed representation of topography and soil properties, whereas the atmospheric resolutions are comparable.

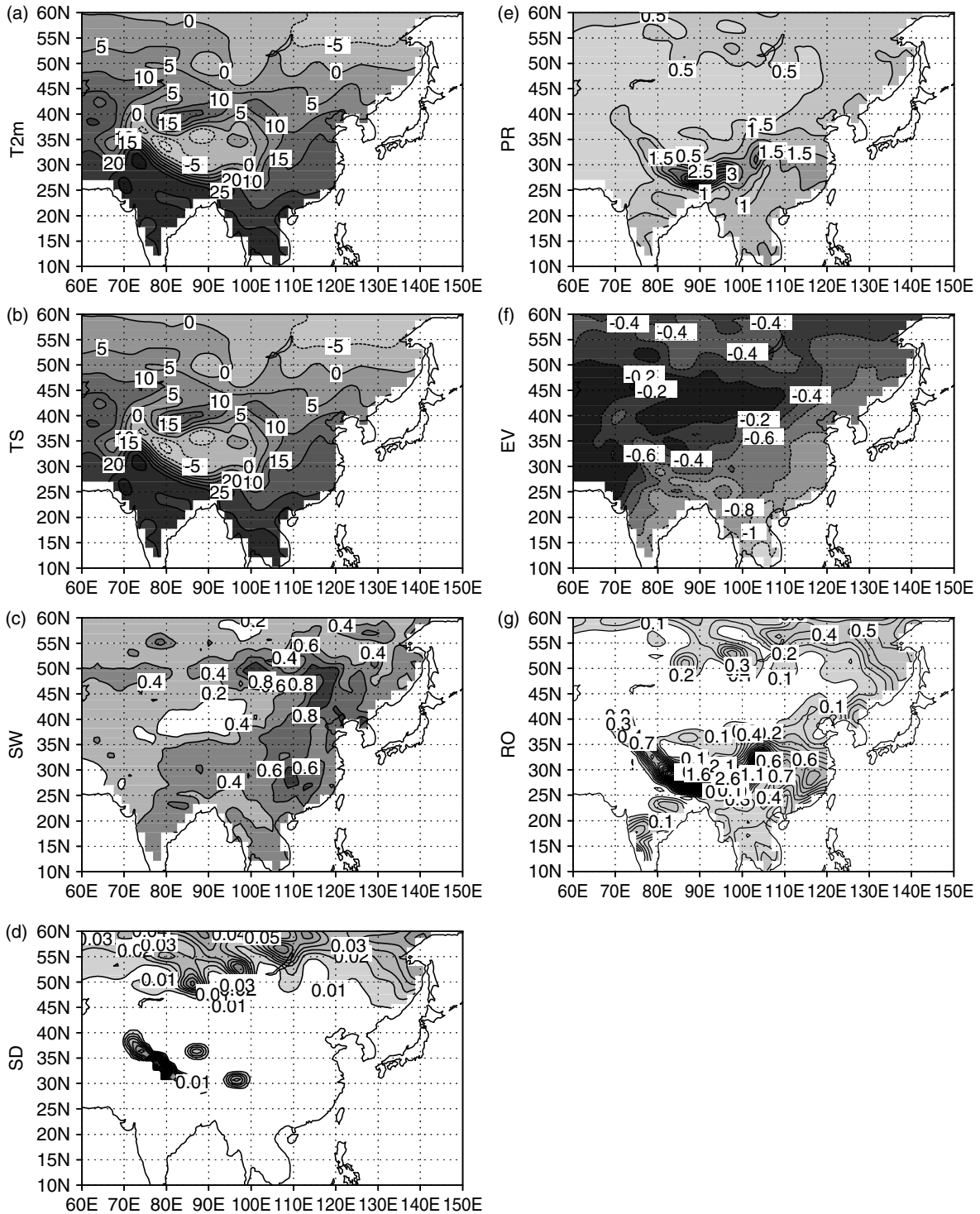


Figure 11. Mean of the simulated climate (standard deviation in Figure 12, mean in NCEP see Figure 13): (a) the near-surface temperature T2m [C], (b) soil temperature [C], (c) soil wetness [m], (d) snow depth [m], (e) precipitation [m/year], (f) evaporation [m/year], and (g) runoff [m/year]. Contour intervals are 5C (a,b), 0.2 m (c), 0.01 m (d), 0.5 m/year (e), 0.2 m/year (f,g)

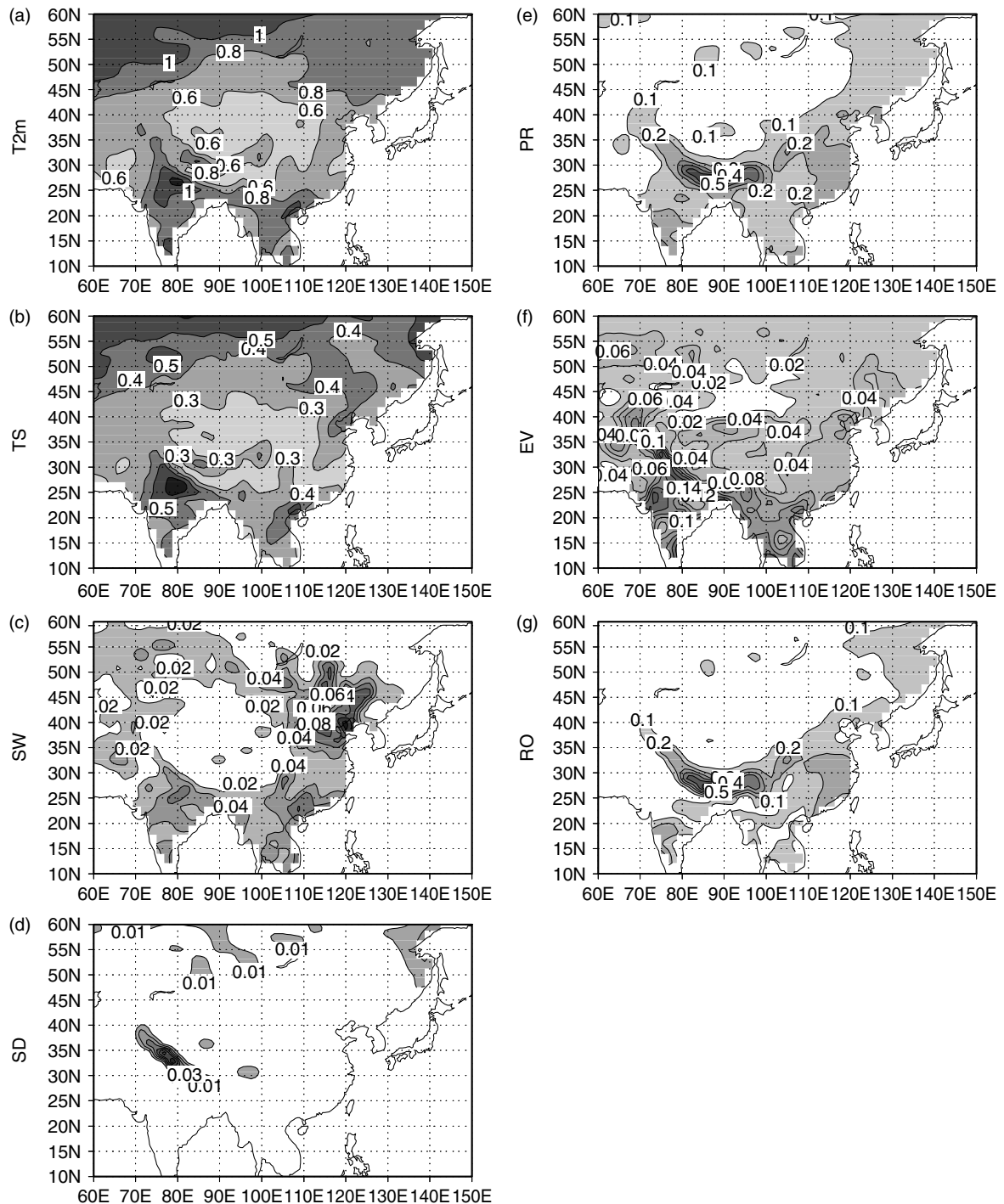


Figure 12. Standard deviation of the simulated annual climate (means see Figure 11, standard deviation in NCEP see Figure 14): (a) near-surface temperature T2m [C], (b) soil temperature [C], (c) soil wetness [m], (d) snow depth [m], (e) precipitation [m/year], (f) evaporation [m/year], and (g) runoff [m/year]. Contour intervals are 0.2C (a), 0.1C (b), 0.02 m (c), 0.01 m (d), 0.1 m/year (e,g), 0.02 m/year (f)

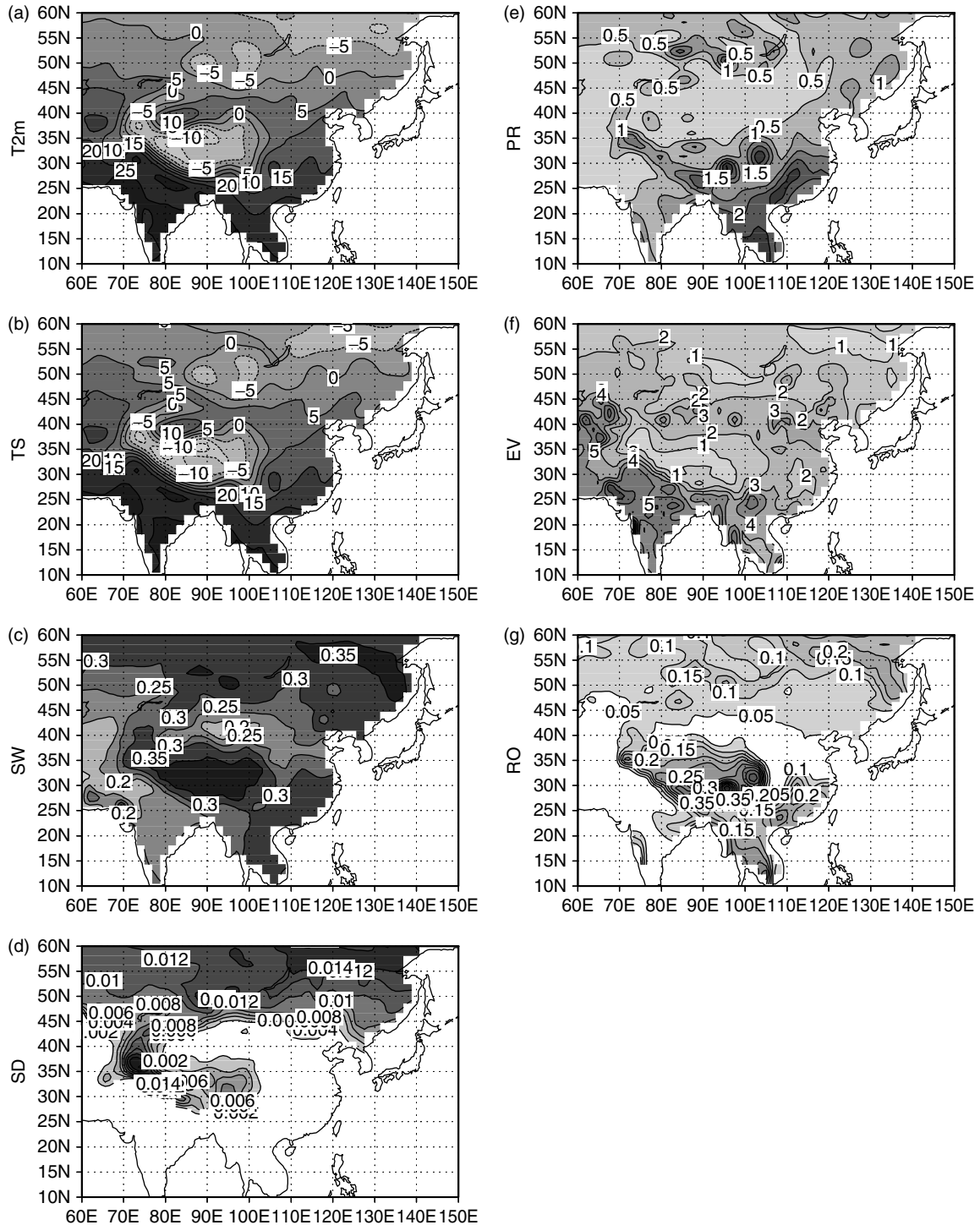


Figure 13. Mean of the observed climate in NCEP (standard deviation see Figure 14, mean of the simulation see Figure 11): (a) the near-surface temperature T2m [C], (b) soil temperature [C], (c) soil wetness [volume fraction, %], (d) snow depth [m], (e) precipitation [m/year], (f) potential evaporation [m/year], and (g) runoff [m/year]. Contour intervals are 5C (a,b), 0.05 m (c), 0.005 m (d), 0.5 m/year (e), 1 m/year (f), 0.05 m/year (g)

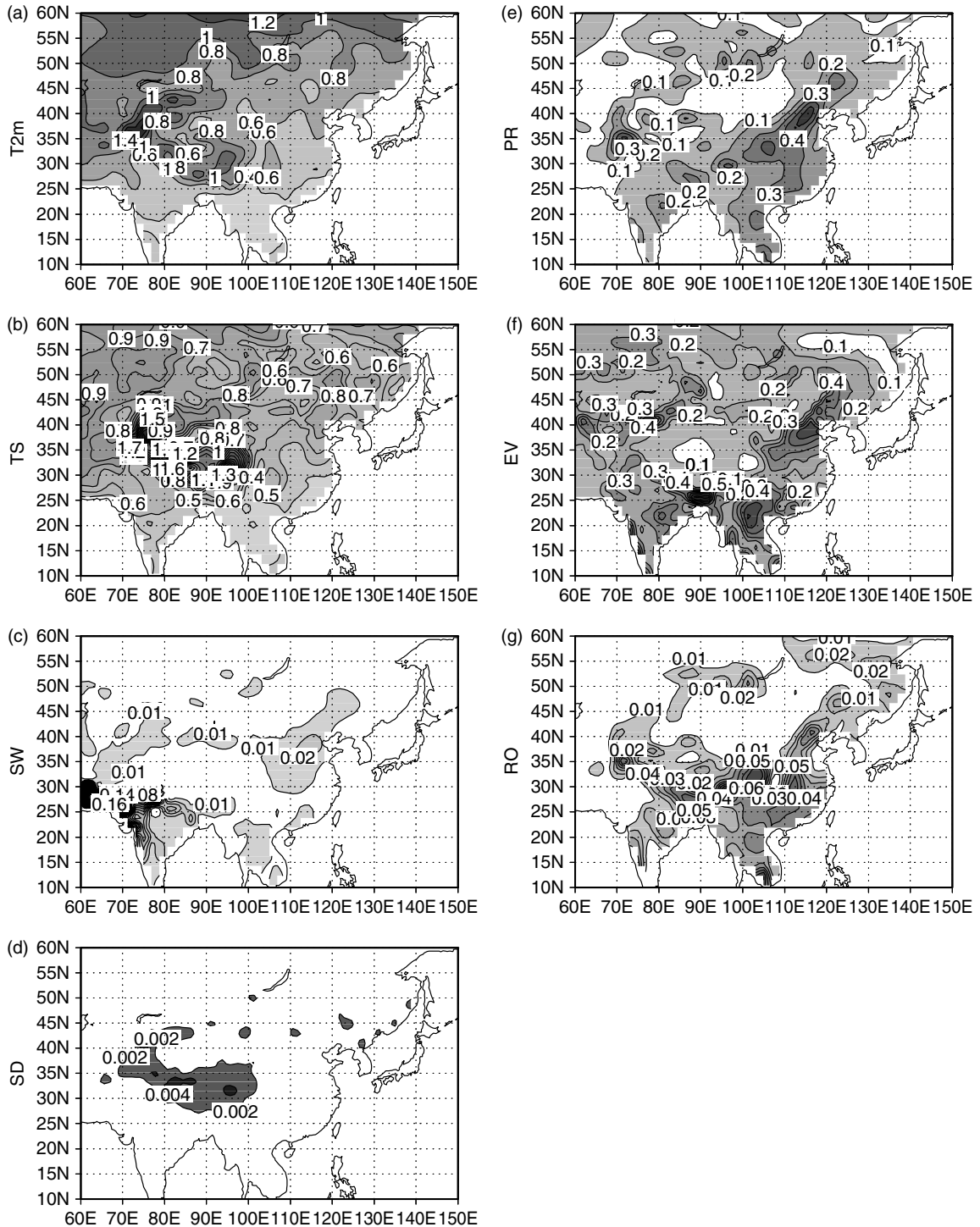


Figure 14. Standard deviation of the observed annual climate in NCEP (see Figure 13 for the means, see Figure 12 for the standard deviation in the simulation): (a) near-surface temperature T2m [C], (b) soil temperature [C], (c) soil wetness [volume fraction, %], (d) snow depth [m], (e) precipitation [m/year], (f) potential evaporation [m/year], and (g) runoff [m/year]. Contour intervals are 0.2C (a), 0.1C (b), 0.02 m (c), 0.002 m (d), 0.1 m/year (e, f), 0.02 m/year (g)

Therefore, we restrict the discussion to the most relevant features of the simulated climate and the differences with respect to the NCEP reanalysis on a point-by-point basis (Figures 11, 12, 13, and 14):

1. Near-surface air (2m) temperature: Whereas the means coincide (Figures 11(a), 13(a)), the variabilities, although of similar magnitudes, show different spatial centres (Figures 12(a), 14(a)).
2. Soil temperature: The simulated mean agrees with NCEP (Figures 11(b), 13(b)), while the standard deviation (Figures 12(b), 14(b)) appears to be underestimated in the Pamir/Himalaya region (35N, 70–100E) by the model.
3. Soil wetness: There is little correspondence of simulated and NCEP means and variances (Figures 11(c), 13(c), and 12(c), 14(c)), which can be explained by the different setups. The few independent and direct observations of soil wetness in China during 1981–1999 (Li *et al.*, 2005), although scattered over a wide area, support the large gradients in the simulation. The high variability of soil wetness in the NCEP data in the area of Afghanistan is not simulated.
4. Snow depth: Snow depth shows higher means and variabilities in the simulation (Figures 11(d), 12(d)) than in NCEP (Figures 13(d), 14(d)), in particular, the high values in the Hindu Kush and Himalaya regions, and high gradients are not present in NCEP. Note the error in the snowpack of NCEP (Hagemann and Dümenil-Gates, 2001).
5. Precipitation: The simulated mean agrees with NCEP (Figures 11(e), 13(e)) except for South East China, where NCEP overestimates the monsoon (Hagemann and Dümenil-Gates, 2001). In this region the simulated variability appears to be underestimated (Figures 12(e), 14(e)).
6. Evaporation: The potential evaporation available in NCEP can serve as an upper bound for evaporation; further assessment is beyond the present study. The comparison of the simulated evaporation with the reanalysed potential evaporation shows little agreement in the means (Figures 11(f), 13(f)) and variances (Figures 12(f), 14(f)).
7. Runoff: The simulated runoff is much more concentrated in the Yangtze and the Huang He catchments than in the NCEP data (Figures 11(g), 13(g)), whereas the variability is of comparable magnitude (Figures 12(g), 14(g)).

#### REFERENCES

- Blender R, Fraedrich K. 2003. Long time memory in global warming simulations. *Geophysical Research Letters* **30**: 7(1–4).
- Bordi I, Sutera A. 2004. Drought variability and its climatic implications. *Global and Planetary Change* **40**: 115–127.
- Bordi I, Fraedrich K, Jiang JM, Sutera A. 2004a. Spatio-temporal variability of dry and wet periods in eastern China. *Theoretical and Applied Climatology* **79**: 81–91.
- Bordi I, Fraedrich K, Gerstengarbe FW, Werner PC, Sutera A. 2004b. Potential predictability of dry and wet periods: Sicily and Elbe-Basin (Germany). *Theoretical and Applied Climatology* **77**: 125–138.
- Bueh C, Cubasch U, Hagemann S. 2003. Impacts of global warming on changes in the East Asian monsoon and the related river discharge in a global time slice experiment. *Climate Research* **24**: 47–57.
- Fekete BM, Vorosmarty CJ, Roads JO, Willmott CJ. 2004. Uncertainties in precipitation and their impacts on runoff estimates. *Journal of Climate* **17**: 294–304.
- Fraedrich K. 2002. Fickian diffusion and Newtonian cooling: A concept for noise induced climate variability with long-term memory? *Stochastics and Dynamics* **2**: 403–412.
- Fraedrich K, Blender R. 2003. Scaling of atmosphere and ocean temperature correlations in observations and climate models. *Physical Review Letters* **90**: 108501(1–4).
- Fraedrich K, Luksch U, Blender R. 2004. 1/f-model for long time memory of the ocean surface temperature. *Physical Review E* **70**: 037301(1–4).
- Gong DY, Ho CH. 2002. The Siberian high and climate change over middle to high latitude Asia. *Theoretical and Applied Climatology* **72**: 1–9.
- Govindan RB, Vyushin D, Bunde A, Brenner S, Havlin S, Schellnhuber HJ. 2002. Global climate models violate scaling of observed atmospheric variability. *Physical Review Letters* **89**: 28501.
- Hagemann S, Dümenil-Gates L. 2001. Validation of the hydrological cycle of ECHAM and NCEP reanalyses using the MPI hydrological discharge model. *Journal of Geophysical Research* **106**: 1503–1510.
- Hagemann S, Dümenil-Gates L. 2003. Improving a subgrid runoff parameterization scheme for climate models by the use of high resolution data derived from satellite observations. *Climate Dynamics* **21**: 349–359.
- Hurst HE. 1951. Long-term storage capacity of reservoirs. *Transactions of the American Society of Civil Engineers* **116**: 770–799.
- Jiang J, Zhang D, Fraedrich K. 1997. Historic climate variability of wetness in east China (1960–1992): A wavelet analysis. *International Journal of Climatology* **17**: 969–981.
- Jungclaus JH, Botzet M, Haak H, Keenlyside N, Luo J-J, Latif M, Marotzke J, Mikolajewicz U, Roeckner E. 2005. Ocean circulation and tropical variability in the coupled model ECHAM5/MPI-OM. *Journal of Climate* [accepted].

- Kalnay E, Kanamitsu M, Kistler R, Collins W, Deaven D, Gandin L, Iredell M, Saha S, White G, Woollen J, Zhu Y, Leetmaa A, Reynolds B, Chelliah M, Ebisuzaki W, Higgins W, Janowiak J, Mo KC, Ropelewski C, Wang J, Jenne R, Joseph D. 1996. The NCEP/NCAR 40 year reanalysis project. *Bulletin of the American Meteorological Society* **77**: 437–471.
- Legutke S, Maier-Reimer E. 1999. Climatology of the HOPE-G Global ocean-sea ice general circulation model. Technical Report No. 21. Modellberatungsgruppe, DKRZ (Deutsches Klimarechenzentrum): Hamburg.
- Li H, Robock A, Liu S, Mo X, Viterbo P. 2005. Evaluation of reanalysis soil moisture simulations using updated Chinese soil moisture observations. *Journal of Hydrometeorology* **6**: 180–193.
- Liang XZ, Samel AN, Wang WC. 2002. China's rainfall interannual predictability: Dependence on the annual cycle and surface anomalies. *Journal of Climate* **15**: 2555–2561.
- Lin X, Yin ZY. 2001. Spatial and temporal variation of summer precipitation over the eastern Tibetan plateau and the North Atlantic oscillation. *Journal of Climate* **14**: 2896–2909.
- Livina VN, Ashkenazy Y, Braun P, Monetti R, Bunde A, Havlin S. 2003. Nonlinear volatility of river flux fluctuations. *Physical Review E* **67**: 042101.
- Milly PCD, Wetherald RT, Dunne KA, Delworth TL. 2002. Increasing risk of great floods in a changing climate. *Nature* **415**: 514–517.
- Moringa Y, Tian SF, Shinoda M. 2003. Winter snow anomaly and atmospheric circulation in Mongolia. *International Journal of Climatology* **23**: 1627–1636.
- Peng CK, Buldyrev SV, Havlin S, Simons M, Stanley HE, Goldberger AL. 1994. On the mosaic organization of DNA sequences. *Physical Review E* **49**: 1685–1689.
- Qian WH, Chen D, Zhu Y, Shen HY. 2003a. Temporal and spatial variability of dryness/wetness in China during the last 530 years. *Theoretical and Applied Climatology* **76**: 13–29.
- Qian YF, Zheng YQ, Zhang Y, Miao MQ. 2003b. Responses of China's summer monsoon climate to snow anomaly over the Tibetan plateau. *International Journal of Climatology* **23**: 593–613.
- Roads J. 2003. The NCEP-NCAR, NCEP-DOE, and TRMM tropical atmospheric hydrological cycles. *Journal of Hydrometeorology* **4**: 826–840.
- Roeckner E, Bäuml G, Bonaventura L, Brokopf R, Esch M, Giorgetta M, Hagemann S, Kirchner I, Kornbluh L, Manzini E, Rhodin A, Schlese U, Schulzweida U, Tompkins A. 2003. The atmospheric general circulation model ECHAM 5. Technical Report, PART I: Model description MPI Report No. 349. Max-Planck-Institute for Meteorology: Hamburg.
- Wang JXL, Gaffen DJ. 2001. Late-twentieth-century climatology and trends of surface humidity and temperature in China. *Journal of Climate* **14**: 2833–2845.
- Wang R, Wang S, Fraedrich K. 1991. An approach to reconstruction of temperature on a seasonal basis using historical documents from China. *International Journal of Climatology* **11**: 381–392.
- Wolff JO, Maier-Reimer E, Legutke S. 1997. The Hamburg ocean primitive equation model HOPE. Technical Report No. 13. Deutsches Klimarechenzentrum: Hamburg.